



# Atomistic Models for Highly-Dispersed PtSn/ $\gamma$ -Al<sub>2</sub>O<sub>3</sub> Catalysts: Ductility and Dilution Affect the Affinity for Hydrogen

Agnès Gorczyca, Pascal Raybaud, Virginie Moizan, Yves Joly, Céline Chizallet

## ► To cite this version:

Agnès Gorczyca, Pascal Raybaud, Virginie Moizan, Yves Joly, Céline Chizallet. Atomistic Models for Highly-Dispersed PtSn/ $\gamma$ -Al<sub>2</sub>O<sub>3</sub> Catalysts: Ductility and Dilution Affect the Affinity for Hydrogen. ChemCatChem, 2019, 11 (16), pp.3941-3951. 10.1002/cctc.201900429 . hal-02276526

**HAL Id: hal-02276526**

**<https://hal.science/hal-02276526>**

Submitted on 6 Dec 2019

**HAL** is a multi-disciplinary open access archive for the deposit and dissemination of scientific research documents, whether they are published or not. The documents may come from teaching and research institutions in France or abroad, or from public or private research centers.

L'archive ouverte pluridisciplinaire **HAL**, est destinée au dépôt et à la diffusion de documents scientifiques de niveau recherche, publiés ou non, émanant des établissements d'enseignement et de recherche français ou étrangers, des laboratoires publics ou privés.

# Atomistic models for highly-dispersed PtSn/ $\gamma$ -Al<sub>2</sub>O<sub>3</sub> catalysts : ductility and dilution affect the affinity for hydrogen

Agnès Gorczyca,<sup>[a,b]</sup> Pascal Raybaud,<sup>[a]</sup> Virginie Moizan,<sup>[a]</sup> Yves Joly,<sup>[b]</sup> Céline Chizallet<sup>\*,[a]</sup>

[a] Dr. A. Gorczyca, Dr. V. Moizan, Dr. P. Raybaud, Dr. C. Chizallet  
IFP Energies nouvelles  
Rond-Point de l'échangeur de Solaize  
BP3, 69360 Solaize, FRANCE  
E-mail: [celine.chizallet@ifpen.fr](mailto:celine.chizallet@ifpen.fr)

[b] Dr. Y. Joly  
Univ. Grenoble Alpes  
CNRS, Institut Néel,  
38042 Grenoble, FRANCE

**Abstract:** Supported platinum-based sub-nanometric particles play a central role in many catalytic applications. In particular, platinum-tin active phases supported on  $\gamma$ -Al<sub>2</sub>O<sub>3</sub> are largely employed for dehydrogenation of alkanes and catalytic reforming of naphta cuts, although geometric and electronic effects of the active phase in the presence of hydrogen still remains highly debated. Thanks to periodic density functional theory (DFT), we propose structural models of such systems containing thirteen metal atoms (Pt<sub>x</sub>Sn<sub>13-x</sub> with  $0 \leq x \leq 13$ ) deposited on the (100)  $\gamma$ -Al<sub>2</sub>O<sub>3</sub> surface. We thus unravel the intricate effects of the composition (Pt/Sn ratio), of the support ( $\gamma$ -Al<sub>2</sub>O<sub>3</sub>) and the hydrogen coverage on the stability of platinum-tin sub-nanometric clusters, in the case where tin is reduced (Sn<sup>0</sup>). A detailed investigation of the interaction of the supported Pt<sub>10</sub>Sn<sub>3</sub> cluster with hydrogen by velocity-scaled molecular dynamics provides a mapping of the hydrogen coverage as a function of the operating conditions (T, P(H<sub>2</sub>)). Our study highlights significant differences between Pt<sub>13</sub> and Pt<sub>x</sub>Sn<sub>13-x</sub> clusters in terms of ductility and dilution (also called ensemble) effects which may be at the origin of the different reactivities usually reported for Pt and PtSn supported catalysts.

## Introduction

The Pt/ $\gamma$ -Al<sub>2</sub>O<sub>3</sub>-like systems, where platinum is in a highly dispersed form (sub-nanometric particles), are of paramount important in heterogeneous catalysis,<sup>[1, 2]</sup> in particular in the presence of H<sub>2</sub>. For some important – often at the industrial scale – applications like hydrogenation of unsaturated hydrocarbons,<sup>[3]</sup> dehydrogenation of light alkanes<sup>[4-8]</sup> or catalytic reforming of naphta,<sup>[9]</sup> tin is added to improve the selectivity, stability and regeneration properties of the catalysts.<sup>[10]</sup> Yet these effects remain poorly understood at the molecular scale due to some resolution limitations of characterization techniques when undertaken operando.

To make progress in this area and allow a better control of the active phase, the elaboration of structural models for bimetallic platinum-tin subnanometric particles supported on  $\gamma$ -alumina, is of fundamental and practical importance. Density functional theory (DFT) calculations are useful in that respect, due to the challenging characterization of supported clusters, that are often sub-nanometric and non-regular in shape.<sup>[5, 11-16]</sup> Significant amount of work has been devoted so far for the proposal of relevant dispersed monometallic Pt/Al<sub>2</sub>O<sub>3</sub> models,<sup>[17]</sup> in particular by some of us in the case of the gamma polymorph of alumina.<sup>[18-20]</sup> The ductility of small platinum clusters (typically, Pt<sub>13</sub>) appears to be very strong,<sup>[19, 21]</sup> in particular in the presence of hydrogen,<sup>[22, 23]</sup> oxygen<sup>[24]</sup> and hydrocarbons<sup>[25-27]</sup> despite the presence of a support. Moreover, it was shown that Pt<sub>13</sub> cluster exhibit a higher adsorption capacity than the infinite Pt(111) surface.<sup>[22, 23]</sup> Experimental findings support these theoretical observations.<sup>[23, 28]</sup> However, only a few theoretical studies deal with bimetallic PtSn nanoclusters,<sup>[14, 29-31, 32]</sup> despite their high practical interest. None of these studies includes at the same time support and environment effects. To the best of our knowledge, with the exception of an earlier study of H<sub>2</sub> interaction with isolated Pt-Sn dimers,<sup>[33]</sup> hydrogen adsorption has been studied on ideal and infinite alloyed Pt<sub>2</sub>Sn surfaces only.<sup>[34-36]</sup>

The surface properties of bimetallic systems with respect to pure compounds were extensively discussed in terms of electronic (ligand) versus dilution (also called ensemble or geometric) effect.<sup>[37, 38]</sup> The former corresponds to the change induced by electronic transfers between metals of different electronegativities, whereas the later means that the dilution of one metal by the other affects the adsorption modes and coverage, in the case where one metal interacts more strongly than the other with a given molecule. In what follows, we will preferentially use the expression dilution (or ensemble) instead of geometric effect which may stand for a broader range of structural phenomena. For extended surfaces, both kinds of effects lead to a lower affinity of platinum-tin for hydrogen as compared to platinum.<sup>[35, 36, 38]</sup> It remains thus of crucial interest to combining this effect of Pt-Sn alloying with the nano-size effect as previously studied for Pt<sub>13</sub> clusters,<sup>[22, 23]</sup> to predict how the structural, electronic, and hydrogen adsorption properties will be affected in the case of a “ductile” cluster, different from a “rigid” extended surface.

The present work proposes a theoretical investigation of the Pt<sub>x</sub>Sn<sub>y</sub>/ $\gamma$ -Al<sub>2</sub>O<sub>3</sub> system, in the case where tin is formally reduced (Sn<sup>0</sup>). These species are likely to exist for PtSn/ $\gamma$ -Al<sub>2</sub>O<sub>3</sub> catalysts, in particular when synthesized by surface organometallic chemistry.<sup>[8, 11, 12, 14, 39-41]</sup> Models for platinum-tin sub-nanometric clusters, for thirteen metal atoms, are proposed (Pt<sub>x</sub>Sn<sub>13-x</sub> with  $0 \leq x \leq 13$ ). This particle size (close to 0.9 nm as shown in our previous work devoted to Pt<sub>13</sub><sup>[22]</sup>) is relevant with respect to experimental dispersions.<sup>[6, 13, 15, 42, 43]</sup> Moreover, 13 is the smallest number of atoms needed to build an icosahedron or a cuboctahedron. Isolated clusters are

simulated thanks to a simulated annealing method, as well as clusters supported on  $\gamma$ -Al<sub>2</sub>O<sub>3</sub>, thanks to the support model established in ref.<sup>[44]</sup> A detailed investigation of the interaction of the supported Pt<sub>10</sub>Sn<sub>3</sub> cluster with hydrogen is then reported, providing a mapping of the hydrogen coverage as a function of the operating conditions (T, P(H<sub>2</sub>)), and giving first insights into the understanding of the reactivities of platinum-tin and platinum catalysts, in terms of geometric and electronic effects.

## Computational Methods

Periodic density functional theory (DFT) calculations were performed using a plane-wave method as implemented in the Vienna Ab initio Simulation Package.<sup>[45]</sup> The exchange-correlation functional was treated within the generalized gradient approximation (GGA) parameterized by Perdew, Burke and Ernzerhof<sup>[46]</sup> (PBE) and the electron-ion interaction was described by the projector augmented wave (PAW) scheme<sup>[47]</sup> with an energy cutoff of 400 eV. Note that corrections for dispersion forces were not included in the present work for two reasons: i) for the sake of consistency with previous studies that we want to make comparison with,<sup>[19, 22]</sup> ii) and because such refinements to the PBE energies and forces were shown to be rather low in the case of PtSn surfaces in interaction with hydrogen.<sup>[36]</sup> The situation might be more critical for the quantification of the interaction with hydrocarbons,<sup>[27, 36, 48]</sup> which we do not consider here, or for the description of the metal-support adhesion in some cases.<sup>[49]</sup> Spin-polarized calculations were performed for non-supported clusters and used the interpolation formula of Vosko, Wilk and Nusair.<sup>[50]</sup> For isolated metallic clusters, order 1 Methfessel-Paxton smearing with  $\sigma = 0.1$  eV was applied.<sup>[51]</sup> Gaussian smearing with  $\sigma = 0.02$  eV was used for clusters supported on gamma-alumina models. The criterion for the convergence of the self-consistent cycles was set to  $10^{-6}$  eV. Bader charges<sup>[52]</sup> were calculated at the same level of theory. Geometry optimizations were run until forces on relaxed atoms were lower than  $2 \cdot 10^{-2}$  eV.Å<sup>-1</sup>. Dipolar correction was added for non-symmetric slabs in the direction perpendicular to the slab.

Isolated Pt<sub>x</sub>Sn<sub>13-x</sub> clusters ( $0 \leq x \leq 13$ ) were optimized in a  $20 \times 20 \times 20$  Å<sup>3</sup> cubic cell and the corresponding Brillouin-zone k-point mesh sampling was restricted to the gamma point. In the same spirit as our previous works on monometallic clusters,<sup>[22, 23, 53]</sup> a simulated annealing method was applied to find the most stable Pt<sub>x</sub>Sn<sub>13-x</sub> clusters by scanning a large structural configuration space. This simulated annealing method is based on first-principles NVT velocity scaled molecular dynamics (MD) followed by quenches at 0 K. The whole simulation time was at least 20 ps and the time for each step was set to 10 fs. Several simulation temperatures were tried (between 400 and 1200 K), as well as several starting geometries (Pt cuboctahedron or biplanar structure, in which 0 to 13 atoms of Pt were substituted by Sn). The binding energy of isolated Pt<sub>x</sub>Sn<sub>13-x</sub> clusters (per metallic atom) is defined by equation (1).

$$E_b(\text{Pt}_x\text{Sn}_{13-x}) = [E(\text{Pt}_x\text{Sn}_{13-x}) - xE(\text{Pt}) - (13-x)E(\text{Sn})]/13 \quad (1)$$

where  $E(\text{Pt}_x\text{Sn}_{13-x})$ ,  $E(\text{Pt})$  and  $E(\text{Sn})$  are the energies of the Pt<sub>x</sub>Sn<sub>13-x</sub> cluster and of a free Pt/Sn atom, respectively. According to this definition, the more negative the binding energy, the more stable the cluster. The formation energy per metallic atom  $\Delta_f E(\text{Pt}_x\text{Sn}_{13-x})$  is defined by equation (2), by analogy with the definition of the standard enthalpy of formation of solid Pt-Sn alloys. The Pt<sub>13</sub> and Sn<sub>13</sub> clusters are used as references, while for solid state thermodynamics the references are the stable states of the elements in standard conditions at 25°C.<sup>[54]</sup>

$$\Delta_f E(\text{Pt}_x\text{Sn}_{13-x}) = \frac{1}{13} \left[ E(\text{Pt}_x\text{Sn}_{13-x}) - \frac{x}{13} E(\text{Pt}_{13}) - \frac{(13-x)}{13} E(\text{Sn}_{13}) \right] \quad (2)$$

Supported Pt<sub>x</sub>Sn<sub>13-x</sub> clusters ( $0 \leq x \leq 13$ ) were modeled, using the dehydrated  $\gamma$ -Al<sub>2</sub>O<sub>3</sub> (100) surface model described previously.<sup>[44]</sup> Indeed, from previous studies about monometallic or bimetallic catalysts,<sup>[13, 22-24, 55]</sup> models involving the  $\gamma$ -Al<sub>2</sub>O<sub>3</sub>(100) dehydrated surface already provided fruitful detailed information. Moreover, this surface exhibits pentacoordinated Al<sup>3+</sup> ions, which were experimentally suggested to stabilize Pt-Sn clusters efficient for propane dehydrogenation.<sup>[43]</sup> Periodic slabs consist of four alumina layers separated by a vacuum thickness corresponding to more than two equivalent empty layers. The two topmost alumina layers were relaxed, as well as all metallic atoms, whereas the two other ones were frozen. For the investigation of the supported Pt<sub>x</sub>Sn<sub>13-x</sub> in the absence of hydrogen, the dimensions of the cells are  $11.14 \times 16.79 \times 21.80$  Å<sup>3</sup> (see supporting information S1), and a  $2 \times 1 \times 1$  k-points mesh was used. Two strategies were adopted to obtain models for the Pt<sub>x</sub>Sn<sub>13-x</sub>/ $\gamma$ -Al<sub>2</sub>O<sub>3</sub>(100) systems: (i) the most stable Pt<sub>x</sub>Sn<sub>13-x</sub> non supported structures found after simulated annealing were deposited on the  $\gamma$ -Al<sub>2</sub>O<sub>3</sub>(100) surface model, close to the most stable cluster location found for the Pt<sub>13</sub> cluster in reference<sup>[19]</sup>, and geometry optimizations were performed; (ii) starting from the most stable morphology of the biplanar Pt<sub>13</sub> cluster supported on  $\gamma$ -Al<sub>2</sub>O<sub>3</sub>(100), 1 to 13 Pt atoms were replaced by Sn, studying several locations for substituted Sn atoms, and geometry optimizations were performed. The binding energy of supported Pt<sub>x</sub>Sn<sub>13-x</sub> clusters, given per metallic atom, is defined by equation (3).

$$E_b(\text{Pt}_x\text{Sn}_{13-x}/\text{Al}_2\text{O}_3) = \frac{[E(\text{Pt}_x\text{Sn}_{13-x}/\text{Al}_2\text{O}_3) - xE(\text{Pt}) - (13-x)E(\text{Sn}) - E(\text{Al}_2\text{O}_3)]}{13} \quad (3)$$

Where  $E(\text{Pt}_x\text{Sn}_{13-x}/\text{Al}_2\text{O}_3)$  and  $E(\text{Al}_2\text{O}_3)$  are the energies of the supported clusters and of the alumina slab, respectively. Similarly to the isolated clusters, we also define the formation energy per metallic atom  $\Delta_f E(\text{Pt}_x\text{Sn}_{13-x}/\text{Al}_2\text{O}_3)$  by equation (4).

$$\Delta_f E(\text{Pt}_x\text{Sn}_{13-x}/\text{Al}_2\text{O}_3) = \frac{1}{13} \left[ E(\text{Pt}_x\text{Sn}_{13-x}/\text{Al}_2\text{O}_3) - \frac{x}{13} E(\text{Pt}_{13}/\text{Al}_2\text{O}_3) - \frac{(13-x)}{13} E(\text{Sn}_{13}/\text{Al}_2\text{O}_3) - E(\text{Al}_2\text{O}_3) \right] \quad (4)$$

The metal-support interaction energy of a Pt<sub>x</sub>Sn<sub>13-x</sub> cluster on the  $\gamma$ -Al<sub>2</sub>O<sub>3</sub> support is calculated by equation (5).

$$E_{\text{Metal-Support}}(\text{Pt}_x\text{Sn}_{13-x}/\text{Al}_2\text{O}_3) = \frac{[E(\text{Pt}_x\text{Sn}_{13-x}/\text{Al}_2\text{O}_3) - E'(\text{Pt}_x\text{Sn}_{13-x}) - E'(\text{Al}_2\text{O}_3)]}{13} \quad (5)$$

$E'(\text{Pt}_x\text{Sn}_{13-x})$  and  $E'(\text{Al}_2\text{O}_3)$  are respectively the energies of the cluster and the alumina slab with their respective geometry when they are interacting with each other. They differ from their most stable geometry when they are separated.

The structure of the supported Pt<sub>10</sub>Sn<sub>3</sub> system was further refined before investigating hydrogen adsorption, by extending the cell to 16.71 Å in the x direction, by adding new initial states before geometry optimization, and adding velocity scaled MD steps (similar as for non-supported clusters), as shown in supporting information S1. The most stable structure found and reported in the following, results from two of these independent MD (the first one starting from the non-doped supported cluster in which 3 atoms were substituted by tin, the second one starting from the non-doped isolated cluster in which 3 atoms were substituted by tin, then supported) runs followed by a quench at 0 K.

Hydrogen adsorption was modeled on the Pt<sub>10</sub>Sn<sub>3</sub>/ $\gamma$ -Al<sub>2</sub>O<sub>3</sub>(100) system. We did not consider in detail the adsorption of H<sub>2</sub> on the alumina support, as it was shown that the (100) surface orientation only weakly interacts with hydrogen.<sup>[56]</sup> The H coverage on the cluster was varied between 2 to 20 hydrogen atoms per cluster, which appeared to be sufficient to saturate the cluster, contrary to the case of the monometallic Pt system which required to simulate up to 36 atoms (see section 3.4.). In a first approach, and in the same spirit as ref.<sup>[22]</sup>, the most stable Pt<sub>10</sub>Sn<sub>3</sub>/ $\gamma$ -Al<sub>2</sub>O<sub>3</sub>(100) system was used as a starting structure, on which hydrogen atoms were adsorbed, and the system was subjected to a velocity scaled MD study. The cluster

morphology showing strong modifications at H coverage higher than 10 atoms per cluster, other investigations were made on a cuboctahedral cluster morphology (see Supporting Information S2) saturated by hydrogen atoms, and then with decreasing hydrogen loading. The cuboctahedron was put in contact with the alumina support, at a similar location as that of the optimal  $\text{Pt}_{10}\text{Sn}_3$  cluster in the absence of hydrogen. At each coverage, velocity scaled MD runs followed by quench steps were undertaken. The average adsorption energy  $\Delta_{\text{ads}}E$  for the adsorption of  $n$  hydrogen atoms is given by  $\text{H}_2$  molecule and calculated thanks to equation (6). It includes the possible contribution of the reconstruction of the cluster upon  $\text{H}_2$  adsorption.

$$\frac{n}{2}\Delta_{\text{ads}}E = E(\text{H}_n\text{Pt}_{10}\text{Sn}_3/\text{Al}_2\text{O}_3) - E(\text{Pt}_{10}\text{Sn}_3/\text{Al}_2\text{O}_3) - \frac{n}{2}E(\text{H}_2) \quad (6)$$

The phase diagram depicting the stability of the system in terms of hydrogen coverage as a function of the temperature and the hydrogen partial pressure, was built by the same method as the one used in references [22, 23]. The evaluation of the chemical potential for  $\text{H}_2$ , assuming an ideal gas behaviour, leads to the estimation of the temperature - pressure domains where each system at a given hydrogen coverage is the most stable.

## Results and Discussion

### 1. Non-supported $\text{Pt}_x\text{Sn}_{13-x}$ cluster models

The simulated annealing sequence described in the methods section leads to a large set of structures, the most stable one for each composition are shown in Figure 1. All clusters exhibit distorted 3D morphologies and only low coordination metal atoms (no central atom contrary to a cuboctahedron or an icosahedron) thus resulting in cage-like structures. Up to 7 tin atoms in the  $\text{Pt}_x\text{Sn}_{13-x}$  cluster ( $6 \leq x \leq 13$ ), the intercalation of Sn atoms in Pt-Pt bonds is favored, without any segregation of tin. The same holds true for platinum, intercalated in Sn-Sn bonds for  $1 \leq x \leq 6$ . Some analogy can be seen with the bulk platinum-tin compounds (supporting information S3). In particular, the bulk  $\text{Pt}_2\text{Sn}_3$  structure exhibits cage-like sub-structures similar to the  $\text{Pt}_6\text{Sn}_7$  and  $\text{Pt}_5\text{Sn}_8$  clusters, whereas the  $\text{PtSn}_4$  bulk structure reveals layers of platinum atoms between Sn layers, as for the Sn-richer clusters (see supporting information S3 for the extraction of cages and layers from the bulk alloy structures). These observations are compatible with previous works for some of the compositions addressed here.<sup>[32, 57]</sup>

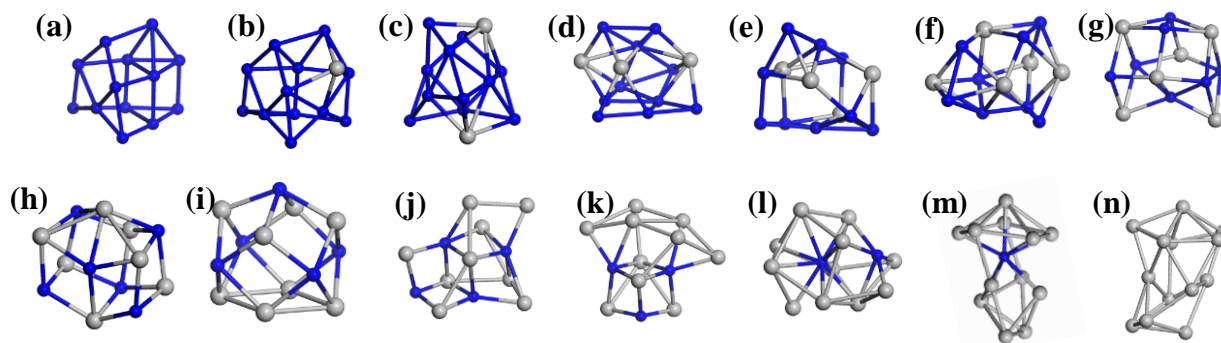


**Figure 1.** Most stable geometry found for  $\text{Pt}_x\text{Sn}_{13-x}$  isolated clusters, after simulated annealing and quenches.  $x$  is equal to: (a) 13, (b) 12, (c) 11, (d) 10, (e) 9, (f) 8, (g) 7, (h) 6, (i) 5, (j) 4, (k) 3, (l) 2, (m) 1, (n) 0. Blue: Pt ; Grey: Sn.

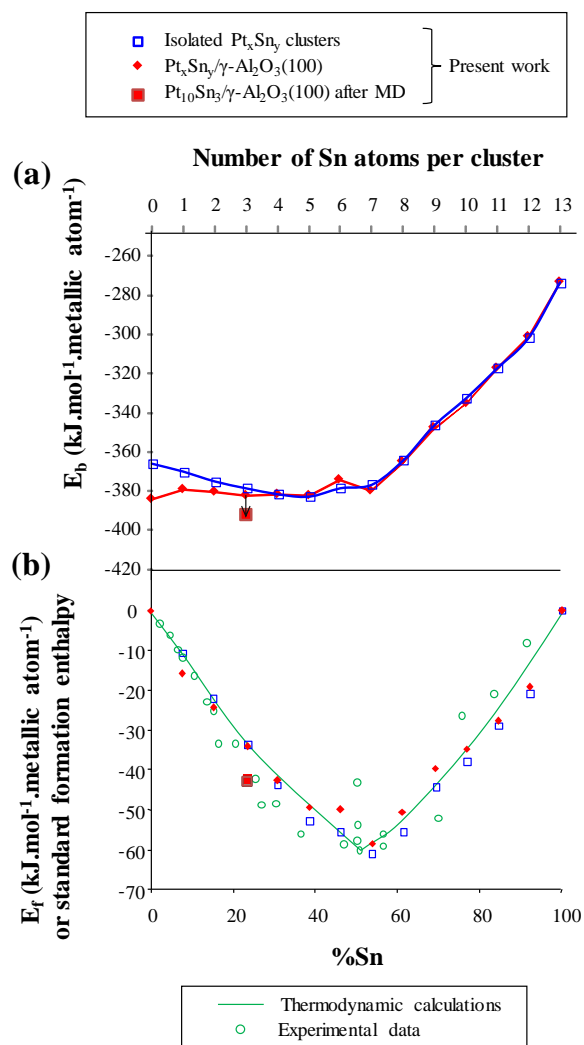


**Figure 2.** (a) Binding energies for non-supported and supported  $\text{Pt}_x\text{Sn}_{13-x}$ , (b) formation energies of the bimetallic clusters with monometallic clusters as reference, together with standard formation enthalpy from the literature (in green) for bulk alloys. Thermodynamic calculations from ref. <sup>[54]</sup>, experimental data from ref. <sup>[54, 58]</sup>

The binding energy (equation (1)) and the formation energy (equation (2)) are reported in Figure 2. The sharp increase of the binding energy starting from 7 tin atoms reveals the low Sn-Sn cohesion as compared to the Pt-Pt one. A shallow minimum in binding energy is however observed close to 5 tin atoms, corresponding to maximal cohesion, indicating the existence of a driving force for the formation of an alloy from isolated atoms. This is confirmed by the evolution of the formation energy (Figure 2-(b)), taking  $\text{Pt}_{13}$  and  $\text{Sn}_{13}$  clusters as references. It is minimal close to 50% Sn, following the same trend as bulk alloys.

Bader charges for the non-supported clusters are reported in section S4. The trends being similar to the one calculated in section 2 for the supported clusters, the reader is referred to the next section for a detailed description. In line with previous reports,<sup>[29, 30, 59, 60]</sup> we find that Pt holds a negative charge in the alloy, making the platinum atoms being in repulsive coulomb interaction one with respect to the other, which likely explains why they do not aggregate in the alloy.<sup>[59]</sup>

## 2. $\text{Pt}_x\text{Sn}_{13-x} / \gamma\text{-Al}_2\text{O}_3(100)$ models

Starting either from the most stable supported  $\text{Pt}_{13}$  geometry (by Sn substitution) or from the most stable  $\text{Pt}_x\text{Sn}_{13-x}$  structures reported in section 1, we obtained the most stable supported structures reported in Figure 3. Their binding energy follows roughly the same trend as the isolated clusters (Figure 2-(a)), except for the lowest tin loading, for which the systems are significantly more stable thanks to the support. This suggests a significantly weaker  $\text{Sn}^0$ -support interaction with respect to the  $\text{Pt}^0$ -support interaction. Indeed, for  $13-x < 6$ , the cluster exhibits a biplanar-like morphology, which is thus strongly reminiscent of the monometallic  $\text{Pt}_{13}$  cluster morphology, whereas at higher Sn loading, the cluster shape is 3D-like, inherited from the simulation of non-supported clusters.

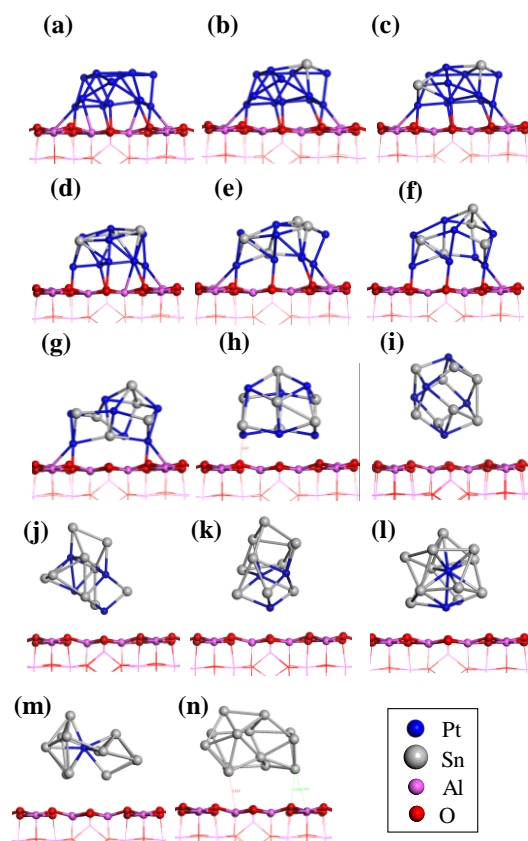


**Figure 3.** Most stable geometry found for supported  $Pt_xSn_{13-x}$  clusters.  $x$  is equal to: (a) 13, (b) 12, (c) 11, (d) 10 (before molecular dynamics investigations), (e) 9, (f) 8, (g) 7, (h) 6, (i) 5, (j) 4, (k) 3, (l) 2, (m) 1, (n) 0.

For all these models except the tin richer ones, tin atoms are well intercalated between the Pt atoms, and prefer to be far away from the support, as compared to platinum, in line with MD reported for supported  $Pt_{10}Sn_{10}$  and  $Pt_{15}Sn_5$  clusters.<sup>[30]</sup> From a structural point of view, the shortest Pt-O and Pt-Al bonds follows three regimes (Figure 4-(a)): up to 6 tin atom per cluster, the values of these minimal distances are close to the one measured in the case of the pure supported platinum cluster (2.1 – 2.2 Å and 2.5 - 2.7 Å for the Pt-O and Pt-Al distance, respectively). These become slightly longer (up to 2.4 Å for Pt-O and 3.3 Å for Pt-Al) for tin richer supported clusters. Indeed, from 7 to 11 Sn in the cluster, the morphology is inherited from the gas phase one, and although a platinum atom is pointing towards the support, a disconnection of the cluster with respect to the support starts to take place. Caballero et al. reported long Pt-O bonds (2.24 Å) for supported PtSn alloys on gamma-alumina,<sup>[12]</sup> which do not appear for the related monometallic Pt system. One may propose that such a contribution is related to the increased metal-support distance due to tin. For the supported  $Pt_1Sn_{12}$  cluster, the platinum atom is occluded inside the cluster by the surrounding Sn atoms so that the distance to the support sharply increases.

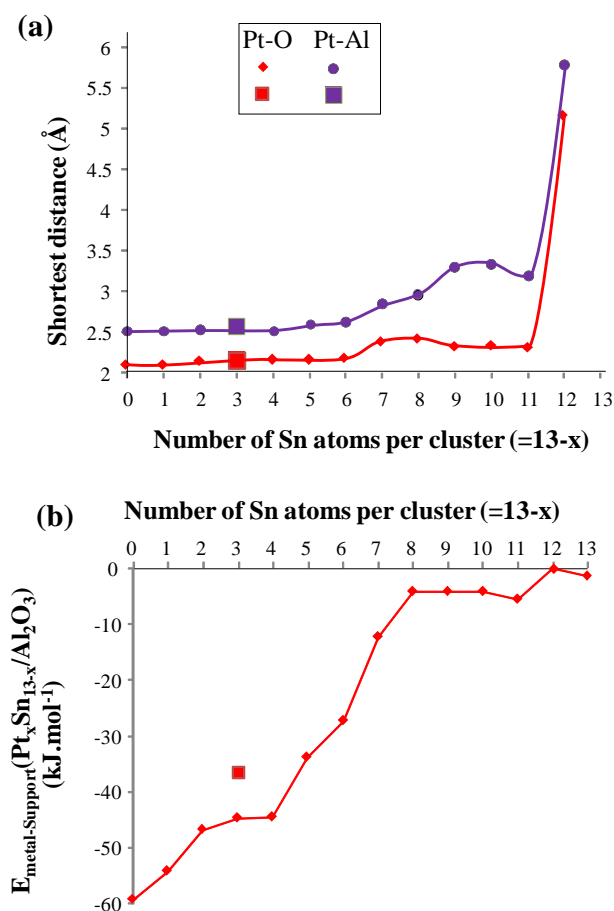


**Figure 4.** (a) Shortest Pt-O and Pt-Al distances and (b) Metal-Support interaction energy in the models of supported Pt<sub>x</sub>Sn<sub>13-x</sub> clusters. The plain squares correspond to the supported Pt<sub>10</sub>Sn<sub>3</sub> cluster after molecular dynamics.

The weakening of the metal-support interaction upon increasing tin loading is further quantified by the metal-support interaction energy, reported in Figure 4-(b), with a nearly zero-interaction starting from 8 tin atoms in the cluster. This can also be seen in Figure 2-(b), where the formation energy of the supported cluster is lower than that of the isolated cluster for low tin loading, the reverse trend being observed at high tin loading. Despite these differences, the formation energy roughly follows the same trend than for other types of alloys.

From an electronic point of view (Figure 5), the clusters are negatively or very slightly positively charged over the whole composition range, which indicates that the support gives electrons to the cluster through the  $\gamma\text{-Al}_2\text{O}_3(100)$  facet, as this was already the case for pure platinum.<sup>[18, 19]</sup> Pt atoms are negatively charged, tin atoms are positively charged, which indicates a charge transfer from Sn atoms to Pt atoms, consistently with the respective electronegativity values of the atomic species (1.8 for Sn and 2.2 for Pt in the Pauling scale<sup>[61]</sup>), with previous computational studies for clusters and surfaces,<sup>[29, 30, 59, 60]</sup> and with XANES experiments.<sup>[12]</sup> Our results also shows that tin tends to be partially oxidized in the nano-alloy. When the tin loading increases, Pt atoms are individually more and more negatively charged, contrary to tin atoms which are less and less positively charged. In other words, the maximal oxidation state per Sn atom is found when one single Sn atom is present in the cluster. The trend is of course symmetrical in the case of Pt for which the maximal charge gain per Pt atom occurs when the cluster contains only one Pt atom. For  $13-x > 8$ , the cluster tends to a neutral state. This can be seen as a consequence of the loss of the metal-support interaction for high loading of tin. Notably, the cumulated charge of Pt and Sn atoms together reaches a minimum, respectively maximum for 7 tin atoms in the cluster, meaning that the overall intensity of the charge transfer is maximal for the close to stoichiometric alloy.

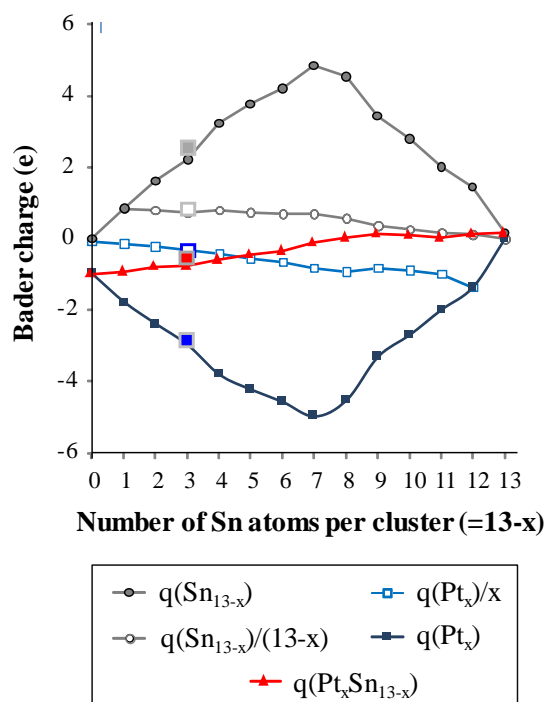


**Figure 5.** Bader charges on the supported  $\text{Pt}_x\text{Sn}_{13-x}/\gamma\text{-Al}_2\text{O}_3(100)$  models. The bigger plain squares depict the Bader charge of the supported  $\text{Pt}_{10}\text{Sn}_3$  cluster after molecular dynamics.

### 3. Refinement of the $\text{Pt}_{10}\text{Sn}_3/\gamma\text{-Al}_2\text{O}_3(100)$ model

Often, during the catalysts synthesis, the Sn and Pt loading are of the same order of magnitude. Nevertheless, previous works suggest that a lower amount of tin is conjectured to be present in the reduced nano-alloy.<sup>[2, 5, 11, 41]</sup> We thus chose the supported  $\text{Pt}_{10}\text{Sn}_3$  cluster, whose stoichiometry is the closest one to the bulk  $\text{Pt}_3\text{Sn}$  one, to simulate hydrogen adsorption. The structure of this system was thus refined (see methods), generalizing the MD procedure to each step of the calculation, whereas preliminary models (section 2) were obtained by geometry optimization only for the supported states. From this approach, one particular cluster morphology showed a superior stability (Figure 6), with a binding energy lowered by  $10 \text{ kJ}\cdot\text{mol}^{-1}$  with respect to the previous geometry optimization (Figure 2-(a)). The resulting refined morphology is closer to the one of the  $\text{Pt}_{13}$  cluster optimized in gas phase (Figure 1-(a)). Compared with the biplanar geometry of the monometallic supported particle (Figure 3-(a)) and that of the  $\text{Pt}_{10}\text{Sn}_3$  supported cluster before MD investigation (Figure 3-(d)), the bimetallic one is more three-dimensional and exhibits 3 stacked atomic layers (5-6-2) instead of the initial bilayer (7-6). The 3 tin atoms are located on the two upmost layers (further from the support) and are surrounded by platinum atoms.

The cluster exhibits 6 Pt-Sn bonds below  $2.7 \text{ \AA}$ , corresponding to an average of  $2.66 \text{ \AA}$  and an average Pt-Sn coordination number of 0.6 (by platinum atom, supporting information S5). Six additional Pt-Sn bonds exist between  $2.7$  and  $3 \text{ \AA}$ , if we include these in the average calculation, the Pt-Sn bond length becomes  $2.71 \text{ \AA}$  for a coordination number (CN) of 1.2. From EXAFS, Siri et al.<sup>[11]</sup> reported Pt-Sn length of the order of  $2.6\text{-}2.7 \text{ \AA}$  for CN between 2.1 and 2.7. Iglesias-Juez et al.<sup>[5]</sup> report Pt-Sn length of  $2.8 \text{ \AA}$  for a CN (per platinum) of 0.7, which appears to be compatible with our calculations. Caballero et al.<sup>[12]</sup> fitted longer ( $2.9 \text{ \AA}$ ) Pt-Sn bonds with lower (1.2) CN, which could be related to the presence of  $\text{Sn}^{\text{II}}$  species. Regarding Pt-Pt bonds, focusing on the 17 bonds shorter than  $3 \text{ \AA}$  (thus an average CN of 1.7), the model exhibits an average length of  $2.67 \text{ \AA}$ , in excellent agreement with several sets of EXAFS experiments.<sup>[11, 12]</sup> Note however that EXAFS was fitted in ref. <sup>[5, 11]</sup> without invoking Pt-O nor Pt-Al bonds, which we have in the model. This may be explained by their amount by platinum atoms (average CN lower than one, see supporting information S5). Other authors need Pt-O bonds to be introduced in the fitting of EXAFS data,<sup>[12]</sup> with Pt-O length close to  $2.24 \text{ \AA}$ , in agreement with our average value of  $2.22 \text{ \AA}$ . The absence of Sn-Sn bonds below  $3 \text{ \AA}$  (the shortest in the model is at  $3.7 \text{ \AA}$ ) is compatible with EXAFS recorded at the K edge of Sn.<sup>[62]</sup>

These structural features result in a higher (lower in terms of absolute value) metal-support interaction (Figure 4-(b)) as compared to the cluster obtained before MD. The enhanced stability of this new model is thus not due to the metal-support interaction, but to a lower deformation energy ( $85$  instead of  $246 \text{ kJ}\cdot\text{mol}^{-1}$  for the refined and non-refined supported  $\text{Pt}_{10}\text{Sn}_3$  models respectively, both referenced to the isolated  $\text{Pt}_{10}\text{Sn}_3$  cluster). In both cases, the interaction between the cluster and the support remains strong to keep the the shortest Pt-O and Pt-Al bond lengths almost unchanged (Figure 4-(a)). The difference in Bader charges before and after the MD procedure is also negligible (Figure 5), suggesting that the main driving force for the charges of Pt and Sn is the alloying effect rather than the support effect.



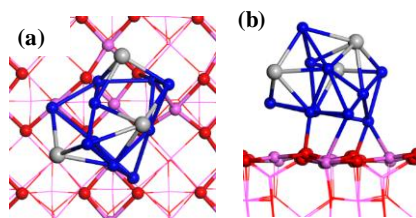


**Figure 6.** Most stable morphology obtained for  $\text{Pt}_{10}\text{Sn}_3/\gamma\text{-Al}_2\text{O}_3(100)$  cluster after the simulated annealing sequence: (a) top view; (b) side view. Same color code as in figure 3.

#### 4. Simulation of hydrogen adsorption on the $\text{Pt}_{10}\text{Sn}_3/\gamma\text{-Al}_2\text{O}_3(100)$ cluster

The hydrogen adsorption study was undertaken on the refined structure of the  $\text{Pt}_{10}\text{Sn}_3/\gamma\text{-Al}_2\text{O}_3(100)$  cluster obtained previously. For that, we chose various starting configurations for the MD simulations for each hydrogen coverage, as explained in the computational section. The most stable structures are reported exhaustively in Supporting information S6, a selection of these being shown in Figure 7. It systematically appears that tin atoms are not favorable sites for hydrogen adsorption, in line with results obtained on flat alloyed surfaces.<sup>[34, 36]</sup> For the system investigated here (in particular, with the (100) alumina surface orientation), H spillover from the cluster to the support was not found to take place spontaneously.

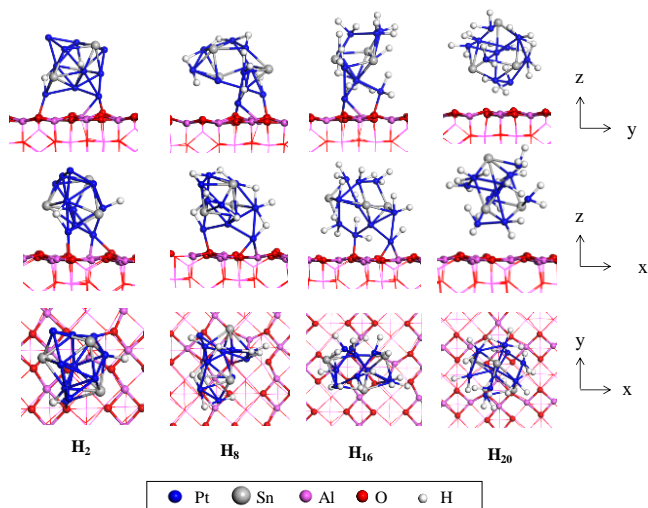


**Figure 7.** Selected most stable structures found for increasing hydrogen coverage on the  $\text{Pt}_{10}\text{Sn}_3/\gamma\text{-Al}_2\text{O}_3(100)$  cluster. Side (along x and y) and top (along z, bottom) views.

The cluster morphology evolved significantly with H adsorption, and is close to the one of a cuboctaedron for 20H. It is remarkable that such a cuboctahedron morphology appeared for  $\text{Pt}_{13}$  in the same range of H atom number adsorbed per cluster.<sup>[22, 23]</sup> For a hydrogen coverage from 2H to 16H, tin atoms are always diluted between Pt atoms, and stay at a significant distance from the support, the shortest Metal-O or Metal-Al bonds always being Pt-O and Pt-Al bonds (Figure 8-a). Thus, the whole cluster keeps connected to the support thanks to Pt-Al (close to 2.4 Å) and Pt-O (close to 2.1 Å) bonds. For 20 H, the distance between the cluster and the support become larger (Figure 8-a).

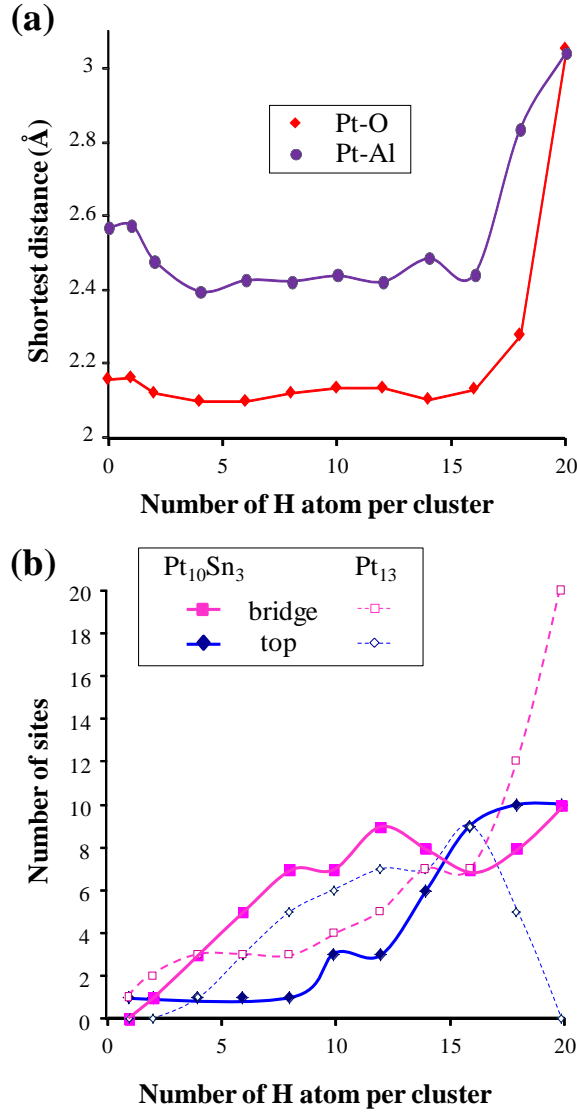


**Figure 8.** (a) Shortest Pt-O and Pt-Al distances and (b) H adsorption mode, function of the number of H atoms adsorbed on the Pt<sub>10</sub>Sn<sub>3</sub>/γ-Al<sub>2</sub>O<sub>3</sub>(100) bimetallic cluster, in comparison with the monometallic Pt<sub>13</sub> cluster (data from [22]). Hollow sites are omitted because they are absent from the Pt<sub>10</sub>Sn<sub>3</sub> cluster and almost absent from the Pt<sub>13</sub> cluster.

The number of top and bridge sites occupied on the most stable systems for a given H coverage are depicted on Figure 8-(b). At low H coverage, excepted for a single hydrogen atom which is preferably adsorbed on top position, the bridge position is largely preferred. For more than 16H adsorbed, there are no bridge sites left due to the intercalation of Sn atoms, then H atoms occupy top sites. For monometallic Pt<sub>13</sub> clusters,<sup>[22]</sup> the trend was different with competing top and bridge sites at hydrogen coverages inferior to 20 H, and with predominant bridge sites at higher hydrogen coverages. However, these high coverages are never reached on the bimetallic cluster simulated here, which is a clear effect of nano-alloying. The lack of bridge sites reveals the geometric effect of tin in the evolution of the properties from pure Pt to Pt alloyed with Sn. Notably, the cuboctaedron obtained at 20 H (Figure 7) contains 12 Pt-Pt edges accessible to hydrogen (symmetrically 12 Sn-Pt edges, i.e. 4 edges per Sn atom). So in principle 12 H atoms can be adsorbed at Pt-Pt bridge sites for the Pt<sub>10</sub>Sn<sub>3</sub> cuboctaedron, versus 24 H for the Pt<sub>13</sub> cuboctaedron. These Sn-Pt bridge position are actually inactive sites for H adsorption. This is also the case for 3 top sites located on Sn. Thus the saturation level is reached for about 20 H atoms, where it was about 36 H atoms. For H coverages higher than 20 H, we observed hydrogen desorption in the course of the MD run (which was not the case for Pt<sub>13</sub>), which also justifies the lower saturation level found for Pt<sub>10</sub>Sn<sub>3</sub>. Considering the important role of bridge sites for both types of clusters, this is likely a key feature to explain the difference between them.

The electrostatic charges were calculated with a Bader analysis for the hydrogenated Pt<sub>10</sub>Sn<sub>3</sub>/γ-Al<sub>2</sub>O<sub>3</sub>(100) (Figure 9). The bimetallic cluster (plus hydrogen atoms) is slightly negatively charged, which shows that it receives electron density from the support. This charge (in absolute value) decreases with increasing the H coverage, so that the whole cluster becomes almost neutral for 20H. This general evolution is similar to that of the Pt<sub>13</sub>/γ-Al<sub>2</sub>O<sub>3</sub>(100) cluster,<sup>[18, 19]</sup> which corresponds to the gradual loss of the covalent metal-support interaction. However, the monometallic cluster (plus H atoms) was intrinsically more negatively charged (-1.1 and -0.7 on the same interval of H) due to the presence of tin which is positively charged. Pt atoms are negatively charged, much more strongly than

in the monometallic cluster, which corresponds to the charge transfer from tin atoms, as a consequence of the respective electronegativity values of platinum and tin (already seen in Figure 5). The charge of platinum atoms is decreasing with the H coverage. H atoms exhibit a weak hydridic nature, with a small negative charge. This result was found also for the biplanar morphology of  $\text{Pt}_{13}$  clusters, in the “low” coverage regime.<sup>[22]</sup> As Sn atoms are positively charged with increasing H coverage, we can deduce that a charge transfer takes place, concomitantly from the support and Sn atoms to Pt and H atoms.

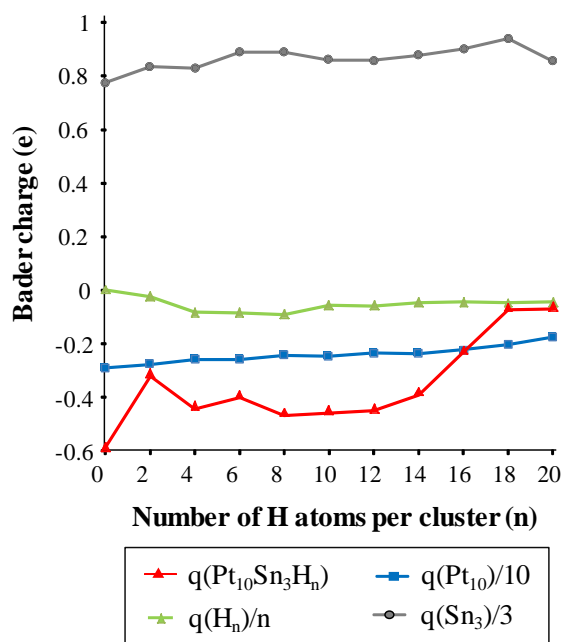


**Figure 9.** Bader charges on the  $\text{H}_n\text{Pt}_{10}\text{Sn}_3/\gamma\text{-Al}_2\text{O}_3(100)$  models. All data are drawn for the most stable cluster structures for a given n value.

A phase diagram was built according to the method described in the computational section, which depicts the evolution of the optimal H coverage as a function of the hydrogen partial pressure and of the temperature (Figure 10). It is compared with the one obtained for the monometallic system,<sup>[22]</sup> and for the  $\text{Pt}_2\text{Sn}/\text{Pt}(111)$  extended surface as modeled by Gautier and Sautet.<sup>[36]</sup> The maximal number of hydrogen atom appearing in the diagram is 16 H by cluster, meaning that the cluster will likely not be disconnected from the support, contrary to what was calculated for  $\text{Pt}_{13}$  supported clusters.<sup>[22, 23]</sup> This could be related to the redispersion role of Sn seen experimentally, although a role of oxidic forms of Sn (not simulated here) can also be thought of in that respect.<sup>[6]</sup>

Comparing the PtSn cluster and the extended surface (Figure 10 (a) and (c) respectively), higher loadings of the clusters are described for given thermodynamics conditions. The zero coverage domain is much larger for the surface, while its maximal loading above 200 K is 0.67 ML (6/9 on the figure). If we define the monolayer on the cluster as the number of hydrogen atom per metallic atom ( $\text{Pt}+\text{Sn}$ ), the maximal coverage appearing on the diagram is 1.23 ML.

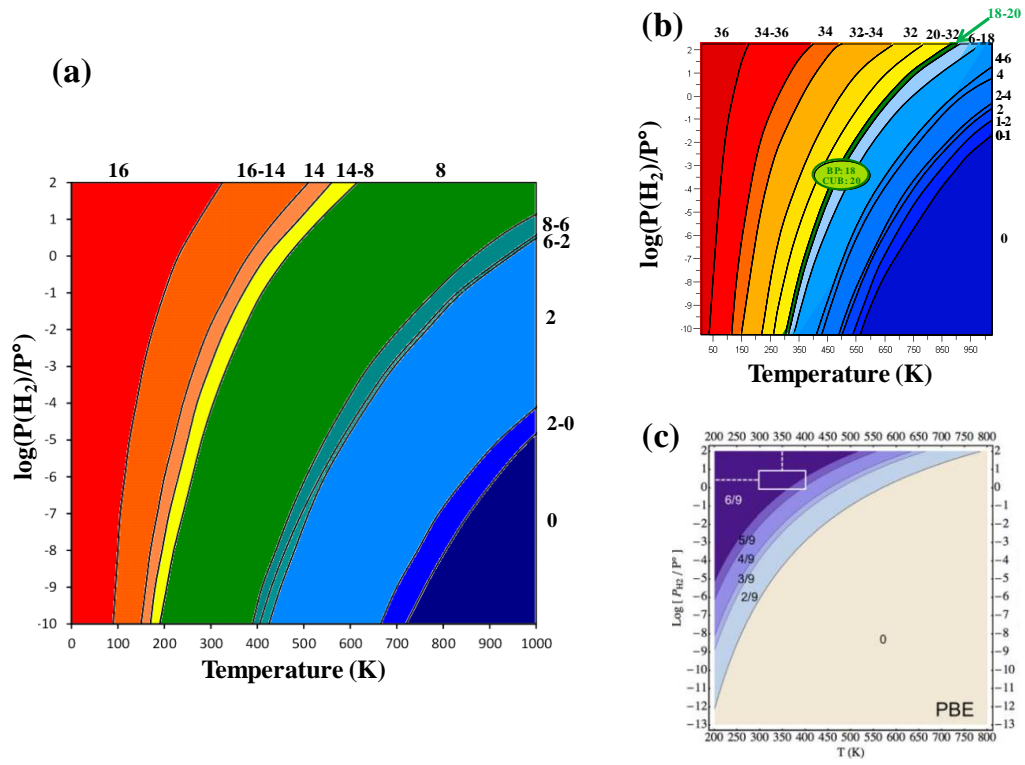


**Figure 10.** Thermodynamic diagrams depicting the most stable hydrogen coverage as a function of the temperature and the hydrogen partial pressure for (a)  $Pt_{10}Sn_3/\gamma-Al_2O_3(100)$ , (b)  $Pt_{13}/\gamma-Al_2O_3(100)$ , adapted from ref. <sup>[22]</sup>, (c) the  $Pt_2Sn/Pt(111)$  extended surface (figure reprinted from ref. <sup>[36]</sup> with permission). For (a) and (b), the number of hydrogen atoms per cluster is given in the corresponding zones. For (a) and (b), all systems within a free adsorption energy difference of 10  $\text{kJ.mol}^{-1}$  are indicated in the given zone. For (c), the coverage is given in monolayer.

Comparing the pure platinum and alloyed clusters, for the high temperature (above 500 K) / low  $H_2$  pressure (below 1 bar) domain, the number of hydrogen atoms on  $Pt_{10}Sn_3$  is generally higher than that of  $Pt_{13}$ . For example, the zero coverage domain is larger in the case of platinum. This may be linked with the experimental observation according to which small amount of tin increase the uptake in  $H_2$  titration experiments.<sup>[63]</sup> This can already be seen from the respective ranking of average adsorption energies between both cluster compositions (Supporting information S7), demonstrating a stronger adsorption of hydrogen for low coverage on  $Pt_{10}Sn_3$  than on  $Pt_{13}$ . This is in contradiction with the electronic effect observed for extended surfaces, which makes the interaction lower for PtSn with respect to Pt.<sup>[35, 36, 38]</sup> Moreover at low coverage the dilution effect does not apply.

The explanation may raise from the larger structural ductility of the  $Pt_{10}Sn_3$  with respect to  $Pt_{13}$ . Indeed, the geometries of the supported  $Pt_{10}Sn_3$  clusters after adsorption of 0, 2 and 8 hydrogen atoms are very different one to another (Figure 7), while for  $Pt_{13}$  the cluster remains biplanar in this range of hydrogen coverage.<sup>[22]</sup> Such a reconstruction cannot take place on infinite surface which may explain why this trend was not observed on  $Pt_2Sn$  surface.<sup>[36]</sup>

However, when lowering the temperature or increasing the hydrogen pressure, the presence of tin drastically reduces the amount of adsorbed hydrogen on the cluster, as compared to pure supported platinum clusters. For example, under  $T = 300$  K and  $P(H_2) = 1$  bar, the H/Pt is at most 1.6 ( $H/(Pt+Sn) = 1.2$ ) for the bimetallic cluster against 2.6 for the monometallic one. This limitation can be directly linked with the dilution of platinum by tin mentioned above. This behavior is compatible several chemisorption and microcalorimetry experiments made for Pt and PtSn systems on various supports.<sup>[15, 39, 63, 64, 65]</sup> Regarding hydrogen adsorption energies (Supporting information S7), a crossing of the curves between  $Pt_{13}$  and  $Pt_{10}Sn_3$  indeed takes place.

The two effects (ductility and dilution effects by PtSn) may have some consequences on the catalytic properties of the clusters. The ductility effect has been recently invoked to be involved in the dehydrogenation mechanisms of  $Pt_{13}$  clusters supported on alumina.<sup>[25, 27]</sup> The formation of the PtSn nano-alloy thus further enhances this ductile character of the cluster with a potential impact on the dehydrogenation reactivity thanks to the stabilization of H atoms at low coverages. On the one hand, the stronger affinity at low coverage may enhance the dehydrogenation steps. On the other hand, since the maximal number of H atoms is diminished (with respect to monometallic cluster) by dilution effect, it is expected that the reverse hydrogenation reaction is limited. Although this qualitative interpretation must be further quantified by dedicated theoretical investigations, we may understand better why alumina supported PtSn catalysts are preferentially used in dehydrogenation and dehydrocyclisation reactions.<sup>[4-8]</sup>

To compare the calculated amounts of hydrogen with experiments, let us focus on the total amount of chemisorbed hydrogen measured evaluated by Singh et al.<sup>[15]</sup> for dispersed Pt and PtSn catalysts supported on alumina. The authors start chemisorption after in situ reduction under  $H_2$ . Prior adsorption of hydrogen, the samples were evacuated under vacuum at 473 K and then cooled down at 303 K. In these conditions, estimating the initial hydrogen coverage is very difficult, as for both catalysts compositions, the phase diagrams suggest a very high sensitivity of the hydrogen coverage upon temperature and pressure. This means that the initial coverage will depend on the vacuum level, and probably also on the duration of the thermal treatments. Let us take the coverage given on the diagram at  $T = 473$  K and  $10^{-4}$  bar of pressure. The expected coverage are close to 20 H for Pt (Figure 10-(b)) and 8 H for PtSn (Figure 10-(a)). The adsorption is then performed at 303 K.<sup>[15]</sup> In these conditions, the maximal number of H atom per cluster is expected to be 36 for Pt and 16 for PtSn. Differentially, this means that  $Pt_{13}$  and  $Pt_{10}Sn_3$  clusters will host close to 16 and 8 H atoms, corresponding to H/Pt ratios of 1.23 and 0.8, in remarkable agreement with the experimental values of 1.25 and 0.75.<sup>[15]</sup> Similar ranking was obtained by Merlen et al.,<sup>[65]</sup> although the absolute values differ a little bit probably due to variations in the treatment conditions before hydrogen chemisorption. Although the evaluation from ab initio calculations is made after several sets of hypotheses, the fact that the order of magnitude is right means that we have captured the main feature leading to the drop of hydrogen adsorption capacity after alloying with tin.

## Conclusions

Thanks to ab initio calculations consisting of geometry optimizations and simulated annealing sequences, we have established a set of  $Pt_xSn_{13-x}$  and  $Pt_xSn_{13-x}/\gamma-Al_2O_3$  models (with  $0 \leq x \leq 13$ ), in the case where tin is formally reduced ( $Sn^0$ ). A considerable diversity of morphologies are described, dependent on the composition of the cluster (Sn/Pt), the effect of the support, and on the hydrogen coverage (investigated for the  $Pt_{10}Sn_3$  stoichiometry). This illustrates the ductility of such sub-nanometer objects.  $Sn^0$  is reluctant to undertake interactions with the alumina support, and does not aggregate for moderate Sn/Pt ratios, giving rise to alloyed systems. A charge transfer results from the formation of the alloy, from Sn to Pt, reinforced on alumina by electron transfer from the support, and electron withdrawing by hydrogen atoms adsorbed on the cluster.

The analysis of hydrogen adsorption geometries and of the adsorption thermodynamic diagram lead us to conclude that at high hydrogen coverage, the availability of bridge adsorption sites is key to explain the lower adsorption capacity of PtSn nano-alloy with respect to Pt. By contrast, at low hydrogen coverage, the higher ductility of the Platinum-Tin cluster is playing a key-role, making PtSn more prone to adsorb hydrogen than Pt. This effect is specific to sub-nanometric particles. These combined effects open the route to the interpretation of the beneficial role of tin in PtSn catalyzed reactions, providing the right balance in terms of Pt/Sn ratio and hydrogen coverage is found. In any case, the behavior of PtSn nano-alloy with respect to H is different from the one of extend surface particularly at low H coverages. As a first perspective, it may be relevant to investigate how this modulation of the nano-alloy cluster affinity for H adsorption may impact the reactivity and mechanisms of dehydrogenation reactions.

Moreover, one should also underline that oxidized forms of tin ( $Sn^{II}$  and  $Sn^{IV}$ ) are known to be present on such catalysts, depending on synthesis parameters such as platinum and tin content and precursors nature, activation/reaction conditions or the presence of heteroatoms.<sup>[5-7, 11-14, 40, 41, 43, 62, 65, 66]</sup> Sn species remaining isolated at the surface support are indeed suspected to play a role in PtSn particles (re)dispersion.<sup>[6]</sup> Our charge analysis reveals that tin is indeed partially oxidized in the alloy, but stronger oxidation may be

reached by considering the interaction of additional oxygen with tin. As a second perspective to this work, accounting for the presence of these species will be necessary in the future to provide a more realistic description of the system. The reduced systems simulated here can be a good starting point for such investigation, in the spirit of previous work done for the description of oxidized forms of supported platinum.<sup>[24]</sup>

## Acknowledgements

The authors are grateful to Prof. Carlo Lamberti (University of Turin), who passed away abruptly on February 1<sup>st</sup>, 2019, for his encouraging and fruitful comments about this work. This work was performed using HPC resources from GENCI-CINES (Grant A0020806134) and from IFP Energies nouvelles. The authors thank S. Lacombe and P. Avenier (IFP Energies nouvelles) for fruitful discussions.

**Keywords:** Nanoparticles • platinum • tin • density functional theory • reconstruction

- [1] H.-J. Freund, *Surf. Sci.*, **2002**, 500, 271-299; B.C. Gates, *Chem. Rev.*, **1995**, 95, 511-522; B. Roldan Cuenya, F. Beharfarid, *Surf. Sci. Rep.*, **2015**, 70, 135-187; W. Karim, C. Spreafico, A. Kleibert, J. Gobrecht, J. VandeVondele, Y. Ekinici, J.A. van Bokhoven, *Nature*, **2017**, 541, 68-71; W. Yu, M.D. Porosoff, J.G. Chen, *Chem. Rev.*, **2012**, 112, 5780-5817.
- [2] P. Avenier, D. Bazer-Bachi, F. Bazer-Bachi, C. Chizallet, F. Deleau, F. Diehl, J. Gornay, É. Lemaire, V. Moizan-Basle, C. Plais, P. Raybaud, F. Richard, S. Lacombe, *Oil Gas Sci. Technol. - Rev. IFPEN*, **2016**, 71, 41-59.
- [3] F. Zaera, *ACS Catal.*, **2017**, 7, 4947-4967.
- [4] O.A. Bariás, A. Holmen, E.A. Blekkan, *Catal. Today*, **1995**, 24, 361-364.
- [5] A. Iglesias-Juez, A.M. Beale, K. Maaijen, T.C. Weng, P. Glatzel, B.M. Weckhuysen, *J. Catal.*, **2010**, 276, 268-279.
- [6] H.N. Pham, J.J.H.B. Sattler, B.M. Weckhuysen, A.K. Datye, *ACS Catal.*, **2016**, 6, 2257-2264.
- [7] N. Kaylor, R.J. Davis, *J. Catal.*, **2018**, 367, 181-193.
- [8] H. Zhu, D.H. Anjum, Q. Wang, E. Abou-Hamad, L. Emsley, H. Dong, P. Laveille, L. Li, A.K. Samal, J.-M. Basset, *J. Catal.*, **2014**, 320, 52-62.
- [9] J.H. Sinfelt, *Catalytic reforming*, in: G. Ertl, E. Knözinger, J. Weitkamp (Eds.) Handbook of Heterogeneous Catalysis, Wiley, Weinheim, **1997**, pp. 1939-1955.
- [10] G.C. Bond, *Metal-Catalyzed Reactions of Hydrocarbons*, Springer, New York, **2005**.
- [11] G.J. Siri, J.M. Ramallo-López, M.L. Casella, J.L.G. Fierro, F.G. Requejo, O.A. Ferretti, *Appl. Catal. A*, **2005**, 278, 239-249.
- [12] A. Caballero, H. Dexpert, B. Didillon, F. LePeltier, O. Clause, J. Lynch, *J. Phys. Chem.*, **1993**, 97, 11283-11285.
- [13] A. Jahel, P. Avenier, S. Lacombe, J. Olivier-Fourcade, J.C. Jumas, *J. Catal.*, **2010**, 272, 275-286.
- [14] A. Jahel, V. Moizan-Baslé, C. Chizallet, P. Raybaud, J. Olivier-Fourcade, J.C. Jumas, P. Avenier, S. Lacombe, *J. Phys. Chem. C*, **2012**, 116, 10073-10083.
- [15] J. Singh, R.C. Nelson, B.C. Vicente, S.L. Scott, J.A. van Bokhoven, *Phys. Chem. Chem. Phys.*, **2010**, 12, 5668-5677.
- [16] J.M. Ramallo-López, G.F. Santori, L. Giovanetti, M.L. Casella, O.A. Ferretti, F.G. Requejo, *J. Phys. Chem. B*, **2003**, 107, 11441-11451.
- [17] V.A. Nasluzov, V.V. Rivanenkov, A.M. Shor, K.M. Neyman, N. Rösch, *Chem. Phys. Lett.*, **2003**, 374, 487-495; V.V. Rivanenkov, V.A. Nasluzov, A.M. Shor, K.M. Neyman, N. Rösch, *Surf. Sci.*, **2003**, 525, 173-183; K. Sohlberg, S. Rashkeev, A.Y. Borisevich, S.J. Pennycook, S.T. Pantelides, *ChemPhysChem*, **2004**, 5, 1893-1897; B. Hinnemann, E.A. Carter, *J. Phys. Chem. C*, **2007**, 111, 7105-7126; C. Zhou, J. Wu, T.J.D. Kumar, N. Balakrishnan, R.C. Forrey, H. Cheng, *J. Phys. Chem. C*, **2007**, 111, 13786-13793; L.G.V. Briquet, C.R.A. Catlow, S.A. French, *J. Phys. Chem. C*, **2009**, 113, 16747-16756; L. Xiao, W.F. Schneider, *Surf. Sci.*, **2008**, 602, 3445; N.A. Deskins, D. Mei, M. Dupuis, *Surf. Sci.*, **2009**, 603, 2793-2807; F. Vila, J.J. Rehr, J. Kas, R.G. Nuzzo, A.I. Frenkel, *Phys. Rev. B*, **2008**, 78, 121404; F. Ahmed, M.K. Alam, A. Suzuki, M. Koyama, H. Tsuboi, N. Hatakeyama, A. Endou, H. Takaba, C.A. Del Carpio, M. Kubo, A. Miyamoto, *J. Phys. Chem. C*, **2009**, 113, 15676-15683; H. Gao, *Chem. Phys. Lett.*, **2016**, 657, 11-17; S. Nigam, C. Majumder, *Appl. Surf. Sci.*, **2017**, 422, 1075-1081.
- [18] C. Mager-Maury, C. Chizallet, P. Sautet, P. Raybaud, *ACS Catal.*, **2012**, 2, 1346-1357.
- [19] C.H. Hu, C. Chizallet, C. Mager-Maury, M. Corral Valero, P. Sautet, H. Toulhoat, P. Raybaud, *J. Catal.*, **2010**, 274, 99-110.
- [20] C. Chizallet, P. Raybaud, *Catal. Sci. Technol.*, **2014**, 4, 2797-2813.
- [21] H. Zhai, A.N. Alexandrova, *J Phys Chem Lett*, **2018**, 9, 1696-1702; G. Sun, P. Sautet, *J. Am. Chem. Soc.*, **2018**, 140, 2812-2820; F.D. Vila, J.J. Rehr, R.G. Nuzzo, A.I. Frenkel, *J Phys Chem Lett*, **2017**, 8, 3284-3288; J.J. Rehr, F.D. Vila, *J. Chem. Phys.*, **2014**, 140, 134701.
- [22] C. Mager-Maury, G. Bonnard, C. Chizallet, P. Sautet, P. Raybaud, *ChemCatChem*, **2011**, 3, 200-207.
- [23] A. Gorczyca, V. Moizan, C. Chizallet, O. Proux, W. Del Net, E. Lahera, J.L. Hazemann, P. Raybaud, Y. Joly, *Angew. Chem., Int. Ed.*, **2014**, 53, 12426 – 12429.
- [24] A. Sangnier, M. Matrat, A. Nicolle, C. Dujardin, C. Chizallet, *J. Phys. Chem. C*, **2018**, 122, 26974-26986.
- [25] P. Raybaud, C. Chizallet, C. Mager-Maury, M. Digne, H. Toulhoat, P. Sautet, *J. Catal.*, **2013**, 308, 328-340.
- [26] M.A. Ha, E.T. Baxter, A.C. Cass, S.L. Anderson, A.N. Alexandrova, *J. Am. Chem. Soc.*, **2017**, 139, 11568-11575.
- [27] W. Zhao, C. Chizallet, P. Sautet, P. Raybaud, *J. Catal.*, **2019**, 370, 118-129.
- [28] A.I. Frenkel, M.W. Cason, A. Elsen, U. Jung, M.W. Small, R.G. Nuzzo, F.D. Vila, J.J. Rehr, E.A. Stach, J.C. Yang, *J. Vac. Sci. Technol. A*, **2013**, 32, 020801; A.I. Frenkel, M.W. Small, J.G. Smith, R.G. Nuzzo, K.O. Kvashnina, M. Tromp, *J. Phys. Chem. C*, **2013**, 117, 23286-23294.
- [29] J. Shen, J.M. Hill, R.M. Watwe, B.E. Spiewak, J.A. Dumesic, *J. Phys. Chem. B*, **1999**, 103, 3923-3934.
- [30] F.D. Vila, J.J. Rehr, S.D. Kelly, S.R. Bare, *J. Phys. Chem. C*, **2013**, 117, 12446-12457.
- [31] Y. Wang, Y. Mi, N. Redmon, J. Holiday, *J. Phys. Chem. C*, **2010**, 114, 317-326; A.W. Hauser, J. Gomes, M. Bajdich, M. Head-Gordon, A.T. Bell, *Phys. Chem. Chem. Phys.*, **2013**, 15, 20727-20734.
- [32] X. Huang, Y. Su, L. Sai, J. Zhao, V. Kumar, *Journal of Cluster Science*, **2015**, 26, 389-409.
- [33] S. Castillo, E. Poulain, V. Bertin, A. Cruz, *Int. J. Quantum Chem.*, **1995**, 56, 207-215.
- [34] J. Fearon, G.W. Watson, *J. Mater. Chem.*, **2006**, 16, 1989-1996.
- [35] F. Vigné, J. Haubrich, D. Loffreda, P. Sautet, F. Delbecq, *J. Catal.*, **2010**, 275, 129-139.
- [36] S. Gautier, P. Sautet, *J. Phys. Chem. C*, **2017**, 121, 25152-25163.

- [37] W.M.H. Sachtler, *Catal. Rev.*, **1976**, *14*, 193-210; G.A. Martin, *Catal. Rev.*, **1988**, *30*, 519-562; V. Ponec, W.M.H. Sachtler, *J. Catal.*, **1972**, *24*, 250-261; J.H. Sinfelt, *Prog. Solid State Chem.*, **1975**, *10*, 55-69; J.H. Sinfelt, *Acc. Chem. Res.*, **1977**, *10*, 15-20; R. Burch, *Acc. Chem. Res.*, **1982**, *15*, 24-31; B. Hammer, J.K. Nørskov, *Surf. Sci.*, **1995**, *343*, 211-220; D. Uzio, G. Berhault, *Catal. Rev.*, **2010**, *52*, 106-131; V. Ponec, *Adv. Catal.*, **1983**, *32*, 149-214; M. Che, C.O. Bennett, *Adv. Catal.*, **1989**, *36*, 55-172; J.K.A. Clarke, A.C.M. Creaner, *Ind. Eng. Chem. Prod. Res. Dev.*, **1981**, *20*, 574-593.
- [38] W.M.H. Sachtler, R.A.V. Santen, *Adv. Catal.*, **1977**, *26*, 69-119.
- [39] R.D. Cortright, J.A. Dumesic, *J. Catal.*, **1994**, *148*, 771-778.
- [40] S.A. Bocanegra, S.R. de Miguel, I. Borbath, J.L. Margitfalvi, O.A. Scelza, *J. Mol. Catal. A*, **2009**, *301*, 52-60.
- [41] C. Vértés, E. Tálas, I. Czakó-Nagy, J. Ryczkowski, S. Göbölös, A. Vértés, J. Margitfalvi, *Appl. Catal.*, **1991**, *68*, 149-159; M. Womes, F. Le Peltier, S. Morin, B. Didillon, J. Olivier-Fourcade, J.C. Jumas, *J. Mol. Catal. A*, **2007**, *266*, 55-64.
- [42] E.J. Jang, J. Lee, H.Y. Jeong, J.H. Kwak, *Appl. Catal. A*, **2019**, *572*, 1-8.
- [43] L. Shi, G.M. Deng, W.C. Li, S. Miao, Q.N. Wang, W.P. Zhang, A.H. Lu, *Angew. Chem., Int. Ed.*, **2015**, *54*, 13994–13998.
- [44] M. Digne, P. Sautet, P. Raybaud, P. Euzen, H. Toulhoat, *J. Catal.*, **2002**, *211*, 1-5; M. Digne, P. Sautet, P. Raybaud, P. Euzen, H. Toulhoat, *J. Catal.*, **2004**, *226*, 54-68.
- [45] G. Kresse, J. Hafner, *Phys. Rev. B*, **1994**, *49*, 14251-14269; G. Kresse, J. Furthmüller, *Comput. Mat. Sci.*, **1996**, *6*, 15-50.
- [46] J. Perdew, K. Burke, M. Ernzerhof, *Phys. Rev. Lett.*, **1996**, *77*, 3865-3868.
- [47] G. Kresse, D. Joubert, *Phys. Rev. B*, **1999**, *59*, 1758-1775.
- [48] S. Gautier, S.N. Steinmann, C. Michel, P. Fleurat-Lessard, P. Sautet, *Phys. Chem. Chem. Phys.*, **2015**, *17*, 28921-28930.
- [49] A.R. Puigdollers, P. Schlexer, G. Pacchioni, *J. Phys. Chem. C*, **2015**, *119*, 15381-15389.
- [50] S.H. Vosko, L. Wilk, M. Nusair, *Can. J. Phys.*, **1980**, *58*, 1200-1211.
- [51] M. Methfessel, A.T. Paxton, *Phys. Rev. B*, **1989**, *40*, 3616-3621.
- [52] E. Sanville, S.D. Kenny, R. Smith, G. Henkelman, *J. Comput. Chem.*, **2007**, *28*, 899-908; G. Henkelman, A. Arnaldsson, H. Jonsson, *Comput. Mat. Sci.*, **2006**, *36*, 354-360.
- [53] C.H. Hu, C. Chizallet, H. Toulhoat, P. Raybaud, *Phys. Rev. B*, **2009**, *79*, 195416.
- [54] V. Grolier, R. Schmid-Fetzer, *J. Alloys Compd.*, **2008**, *450*, 264-271.
- [55] D. Mei, J.H. Kwak, J. Hu, S.J. Cho, J. Szanyi, L.F. Allard, C.H.F. Peden, *J. Phys. Chem. Lett.*, **2010**, *1*, 2688-2691; J.H. Kwak, J. Hu, D. Mei, C.W. Yi, D.H. Kim, C.H.F. Peden, L.F. Allard, J. Szanyi, *Science*, **2009**, *325*, 1670-1673; C. Dessal, A. Sangnier, C. Chizallet, C. Dujardin, F. Morfin, J.L. Rousset, M. Aouine, M. Bugnet, P. Afanasiev, L. Piccolo, *Nanoscale*, **2019**, *11*, 6897-6904.
- [56] R. Wischert, P. Laurent, C. Copéret, F. Delbecq, P. Sautet, *J. Am. Chem. Soc.*, **2012**, *134*, 14430-14449.
- [57] S. Schäfer, B. Assadollahzadeh, M. Mehring, P. Schwerdtfeger, R. Schäfer, *J. Phys. Chem. A*, **2008**, *112*, 12312-12319.
- [58] R. Ferro, R. Capelli, A. Borsese, S. Delfino, *Matematiche e Naturali*, **1973**, *Serie VIII, LIV(4)*, 634-636; H.J. Schaller, *Z. Phys. Chem.*, **1978**, *112*, 85-99; P. Anres, M. Gaune-Escard, J.P. Bros, E. Hayer, *J. Alloys Compd.*, **1998**, *280*, 158-167; S.V. Meschel, O.J. Kleppa, *Thermochim. Acta*, **1998**, *314*, 205-212.
- [59] D.C. Upham, V. Agarwal, A. Khechfe, Z.R. Snodgrass, M.J. Gordon, H. Metiu, E.W. McFarland, *Science*, **2017**, *358*, 917.
- [60] F. Delbecq, P. Sautet, *J. Catal.*, **2003**, *220*, 115-126.
- [61] L. Pauling, *The nature of the chemical bond and the structure of molecules and crystals : an introduction to modern structural chemistry*, Cornell University Press, London, **1960**.
- [62] G. Meitzner, G.H. Via, F.W. Lytle, S.C. Fung, J.H. Sinfelt, *J. Phys. Chem.*, **1988**, *92*, 2925-2932.
- [63] K. Balakrishnan, J. Schwank, *J. Catal.*, **1991**, *127*, 287-306.
- [64] P. Meriaudeau, C. Naccache, A. Thangaraj, C.L. Bianchi, R. Carli, V. Vishvanathan, S. Narayanan, *J. Catal.*, **1995**, *154*, 345-354; F. Coloma, A. Sepúlveda-Escribano, J.L.G. Fierro, F. Rodríguez-Reinoso, *Appl. Catal. A*, **1996**, *148*, 63-80.
- [65] E. Merlen, P. Beccat, J.C. Bertolini, P. Delichère, N. Zanier, B. Didillon, *J. Catal.*, **1996**, *159*, 178-188.
- [66] R. Srinivasan, R.J. De Angelis, B.H. Davis, *J. Catal.*, **1987**, *106*, 449-457; R. Burch, *J. Catal.*, **1981**, *71*, 348-359; J. Olivier-Fourcade, M. Womes, J.-C. Jumas, F. Le Peltier, S. Morin, B. Didillon, *ChemPhysChem*, **2004**, *5*, 1734-1744; M. Boualleg, D. Baudoin, J.M. Basset, F. Bayard, J.P. Candy, J.C. Jumas, L. Veyre, C. Thieuleux, *Chem. Commun.*, **2010**, *46*, 4722-4724; Z. Liu, G.S. Jackson, B.W. Eichhorn, *Angew. Chem. Int. Ed.*, **2010**, *49*, 3173-3176; R. Bacaud, P. Bussière, F. Figueras, *J. Catal.*, **1981**, *69*, 399-409.